Chapter 1
Simulations of Hydrocarbon Polymers Related to Compression Experiments on Sandia's Z Machine

Thomas R. Mattsson, Kyle R. Cochrane, J. Matthew D. Lane and Seth Root

Abstract High-fidelity modeling of hydrocarbon polymers is important for gaining fundamental understanding of the underlying material behavior as well as for designing high energy density (HED) experiments. In this chapter, we describe multi-scale modeling/simulation of hydrocarbon polymers done at Sandia and corresponding experiments on Sandia's Z machine. For polymers, a combination of first-principles simulations using density functional theory (DFT) and atomistic simulations using classical molecular dynamics has proven to effectively model different aspects of the system and we will present both. Throughout, we find that the simulations are in qualitative and quantitative agreement with experiments, suggesting that the hierarchy of simulations can be used to increase our understanding of polymers under dynamic loading conditions.

1.1 Introduction

Hydrocarbon polymers are versatile and therefore ubiquitous materials in experimental loads on high energy density (HED) facilities like the National Ignition Facility (NIF), the Omega laser facility at Laboratory for Laser Energetics (LLE), and the Z machine at Sandia National Laboratories. The physics of polymers span large length- and timescales and the way of modeling polymers has to change to match the different physics. For example, under successively stronger shock compression, polymers melt and dissociate into a hydrogen and carbon fluid/dense plasma. For strong shocks, an accurate modeling of atomic dissociation is important, suggesting that atomistic simulations based on quantum mechanics are the appropriate approach. Polymers are also the building blocks of different types of foams, which have porosity and other internal structure. Foams are extensively used to tailor the behavior in high-pressure experiments not only on a pulsed power driver like the Z machine [41] but also on laser drivers [45]. For foams, an additional scale enters, the scale of pores.

T. R. Mattsson (✉) · K. R. Cochrane · J. M. D. Lane · S. Root
Sandia National Laboratories, Albuquerque, NM 87185, USA
e-mail: trmatts@sandia.gov

N. Goldman (ed.), *Computational Approaches for Chemistry Under Extreme Conditions*, Challenges and Advances in Computational Chemistry and Physics 28,
https://doi.org/10.1007/978-3-030-05600-1_1

For foams, the use of classical molecular dynamics (MD) simulations using reactive force fields has given new insights into formation of hotspots and other aspects of shock dynamics in heterogeneous materials.

The outline of the chapter is as follows. The first section is a discussion on first-principles simulations using density functional theory (DFT), including post-processing to analyze the chemical composition of the material. The second section presents classical MD simulations of hydrocarbon polymers and—foams, we show how the shock propagates in the foam and how local hotspots are formed. In the third section, we discuss Z experimental results on PMP plastic and demonstrate how Z and simulations give a complete picture of the PMP shock response. The chapter concludes with a summary and conclusions.

1.2 First-Principles Simulations of Shocked Polymers

First-principles simulations using Density Functional Theory have brought important insights into how matter behaves under extreme conditions and, importantly, key predictions of thermodynamic properties from DFT simulations have been confirmed experimentally. For example, Sandia's Z machine has been employed to experimentally determine the shock Hugoniot of a number of elements and compounds, including carbon/diamond [25], xenon [47], water [28], carbon dioxide [48], hydrogen [23, 26], krypton [39], and quartz [27]. For these elements and compounds, DFT simulations have been shown to predict the behavior with high fidelity. The DFT modeling of shock compression of hydrogen, carbon, water, carbon dioxide strongly suggests that it is possible to use DFT to successfully simulate hydrocarbon polymers as well. That said, polymers add complexity and the excellent agreement between DFT simulations and experiments demonstrated in 2015 [50] was far from a foregone conclusion.

Density functional theory is based on a theoretical discovery by Walter Kohn [18, 29] that the energy of the electron gas of N electrons can be formulated as a functional of the electron density in real space (3 spatial coordinates) without an explicit use of the wave functions (3 N spatial coordinates, one for each electron). The resulting simplification is tremendous since the problem is reduced from 3 N dimension to 3. The discovery soon resulted in practical quantum simulations of electronic structures of solids, atoms, and molecules. The field has expanded, and DFT simulations are now commonplace across physics, chemistry, biology, and materials science. Although a review of applications of DFT is well outside the scope of this chapter, we will discuss the most important factors of applying DFT to high energy density conditions in general and post-processing for polymers in particular. For a more thorough review on designing DFT calculations for materials science, including HED, please see [37].

1.2.1 First-Principles Thermodynamics of Shock Compression

DFT is applied to problems in physics, material science, and chemistry to calculate the energy in atomic systems. DFT calculations are used to compare energy differences between structures and determine energy barriers between transitions. One of the most common DFT calculations is ionic position optimizations to minimize the system energy and to determine transition paths in the energy landscape. The electronic structure is mostly sought for the lowest, zero Kelvin, energy state, where the Fermi distribution is a step function. The discontinuous Fermi distribution requires extensive k-point sampling of reciprocal space in order to capture the behavior well. Shock compression, on the other hand, involves a discontinuous jump from an initial state to a final state that often is at very high temperature (Fig. 1.1).

Shock physics is driven by the Rankine–Hugoniot (RH) jump conditions, which link the initial and final states for a system with a propagating shock wave of speed u_s and particle velocity after the shock u_p. The RH equations are derived from the conservation of mass, momentum, and energy across the front discontinuity:

$$(P_2 - P_1) = \rho_1(u_s - u_1)(u_2 - u_1) \tag{1.1}$$

$$\rho_{2/}\rho_1 = (u_s - u_1)/(u_s - u_2) \tag{1.2}$$

$$(e_2 - e_1) = \frac{1}{2}(P_2 + P_1)(v_1 - v_2) \tag{1.3}$$

where e is the specific internal energy, P is pressure, and ρ is the density. The subscripts 1 and 2 designate the initial and final states, respectively. The result is a thermodynamics relationship between pressure, specific volume ($v = 1/\rho$), and internal energy of the final and initial states, the so-called Rankine–Hugoniot relationship (1.3) [6].

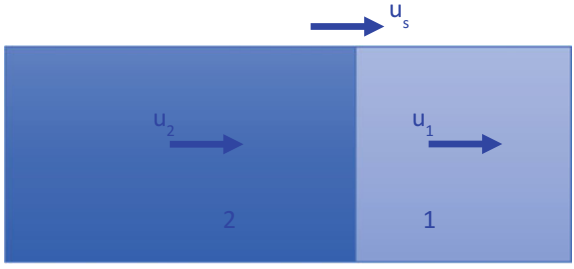

Fig. 1.1 Shock wave in a material, the shock is supersonic and causes a discontinuous transition from thermodynamic state 1 to state 2. The shock velocity is u_s and the net particle velocities before and after the shock are u_1 and u_2. The initial and final states are linked by conservation laws. The analysis can, for example, be made as a thermodynamic control volume

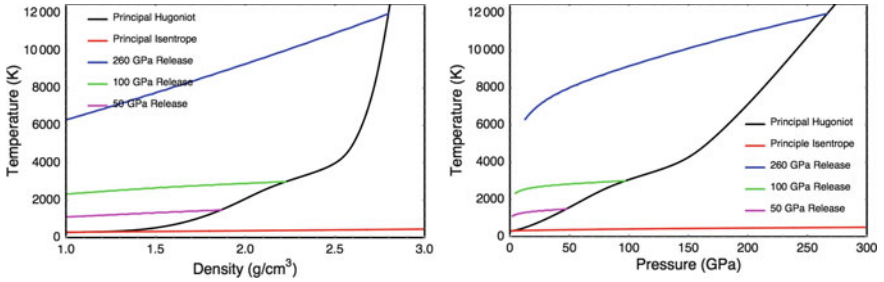

Fig. 1.2 The end states of shock compression of polyethylene [9] (black) and three release paths from different initial shock pressures. Note the shoulder in the Hugoniot between 100 and 150 GPa caused by dissociation of the polymer. Above 150 GPa, there are no longer any molecular fragments, see Fig. 1.7

In thermodynamic space, the loci of end states generated from successively stronger shocks starting from a common initial state are called the Hugoniot. Figure 1.2 shows the polyethylene Hugoniot in density–temperature space (ρ–T) and pressure–temperature (P–T). Figure 1.2 also shows release isentropes: the path the initial shock state relaxes from when the driving pressure is released. Note that the RH equations do not depend on the temperature except via the internal energy. Temperature is extremely difficult to measure experimentally, so there is more uncertainty involving temperature than pressure and density.

The RH energy relationship points toward the need for high accuracy calculations of internal energy and pressure in simulations of shock compression. It is evident that temperature plays a key role, making molecular dynamics (MD) simulations appropriate for sampling the thermodynamics ensemble [1]. At the high temperatures of shock compression, MD is a highly efficient method of sampling the thermodynamic phase space [1].

Importantly, temperature also affects the electronic structure making it necessary to use the Mermin finite-temperature formulation of DFT [42] which involves calculating the full Fermi distribution of electronic states. At high temperature, the full Fermi distribution includes many partially occupied continuum states, requiring significantly more electronic bands than a normal "cold" DFT calculation does. *The consistent use of finite-temperature DFT is one of the most important aspects of performing high-fidelity simulation in the HED regime.*

While the thermal–structural disorder at high temperature relaxes the demands for using a dense k-point sampling compared to that required for calculations of ordered solids at zero Kelvin, it is necessary to apply a high plane-wave cutoff energy in order to converge the electronic pressure [37]. The pressure is calculated with derivatives of the electronic structure and hence converges more slowly than the internal energy. The use of finite-temperature and systematic convergence were two main reasons behind the first high-precision calculations of the deuterium Hugoniot [11]. To summarize, DFT-based molecular dynamics calculations, often referred to as QMD—quantum molecular dynamics—of shock compression requires high

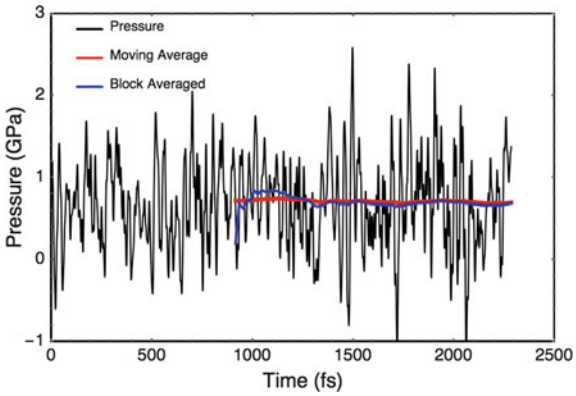

Fig. 1.3 Obtaining thermodynamic information from a long MD simulation. The moving average is a useful measure for when the periodic oscillations in the simulation no longer influence the result. A drift toward lower pressure during the simulation, for example, would indicate relaxation in the system and a longer simulation time is needed

plane-wave cutoff energies, finite-temperature DFT using many partially occupied bands, and the use of pseudo-potentials that are of high quality for normal conditions as well as high-pressure and high-temperature conditions.

Figure 1.3 shows the electronic pressure for a polystyrene simulation at 1.05 g/cc and 300 K. The time step is 0.5 fs. The red line is the moving average of the pressure and is strongly influenced by the correlation between atom positions. In this plot, the initial time for starting the moving average was picked to be close to the estimated mean pressure, so, while the mean of the electronic pressure is 0.67 ± 0.015 GPa, this is misleading as picking a different starting position will yield the same standard deviation but a different mean until many more time steps. Block averaging is a powerful way of extracting uncertainties from correlated data [1]. In this case, the block size used was 37 but made little difference between 20 and 45. The block averaged mean is 0.70 ± 0.08 GPa.

1.2.2 Analysis of Chemical Composition—Tracking Bonds

Of particular importance to simulation of polymers compared to elements is the presence of covalent bonds and the energy associated with bond breaking. The breaking of covalent bonds takes energy, energy that otherwise would be available for increasing the temperature of the shocked material. The result on the Hugoniot curve is the shoulder in temperature evident in Fig. 1.2 at 2.25 g/cm^3 / 120 GPa. In this section, we present a way of identifying molecular structure and apply it to conditions commonly created by strong shock waves in polymer systems.

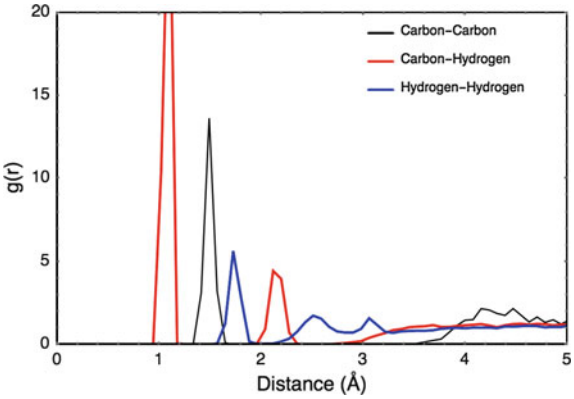

Fig. 1.4 Species-dependent pair correlation function for ethane at 0.571 g/cm^3 and 300 K. The pair correlation plateaus at 1.00 since the pair correlation function is normalized to the random probability of finding an atom in space, hence without any correlation the value is 1.00

Tracking bonds in a simulation is a three-step process. We determine bond lengths, determine bond times, and then, based on those lengths and times, identify and track the bonded atoms. Atoms are considered bonded if they stay within a given distance of each other for a defined amount of time. If, at any time, one of the atoms drifts outside of the prescribed distance and then drifts back in, the time is reset to zero and must again be satisfied.

To determine bond length, we use the species-dependent pair correlation function g(r) to find the distribution of distances between atoms in the reference system, usually at ambient density and temperature. Figure 1.4 shows the pair correlation function of carbon to carbon, carbon to hydrogen, and hydrogen to hydrogen for ethane at 0.571 g/cm^3 and 300 K. These simulations are several picoseconds long, so we use multiple averaging times to obtain different samplings which allow us to check that we do not have a large variation between each averaging time. We then use these values in the bond tracking method on the reference system to confirm that it yields the species of the initial state. Because we use a finite time step and have a small number of atoms, we find that first minimum of the pair correlation for each species is the best choice for bond lengths.

For the following example, we incremented the density of ethane from 0.6 to 4.0 g/cm^3 by 0.1 g/cm^3 and equilibrated each simulation at that density and constant temperature in order to map out the Hugoniot locus points. When the Hugoniot developed a slope inflection, which is often indicative of the onset of dissociation, we calculated the pair correlation on the simulation just prior to the inflection density to confirm that the molecules were still intact. This can be seen in Fig. 1.5. The carbon–carbon bond length is the same. However, the carbon–hydrogen bond is slightly longer, changing from 1.19 to 1.28 Å. Because these values are taken from simulations closer to the dissociation regime in question, these are the values that would be used for the bond tracking.

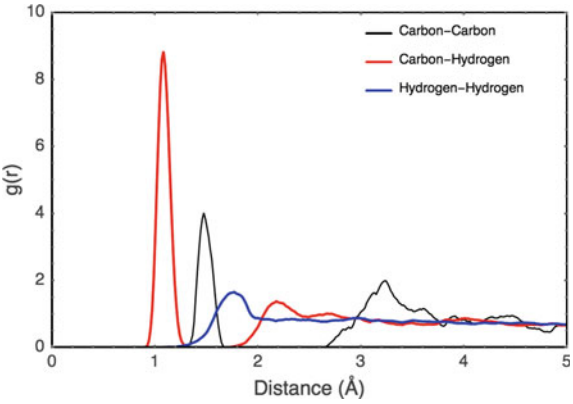

Fig. 1.5 Species-dependent pair correlation function for ethane at 1.2 g/cm^3 and 1050 K. The probability approaches the random value 1.00 at a shorter distance—reflecting less correlation in the positions of atoms than at lower temperature

The next step is to determine the amount of time atoms must be in close proximity to each other to be considered bonded. To start, we run the tracker on the simulation in question and vary the C–C bond distance, C–H bond distance, H–H bond distance, and time requirement.

At 1.5 g/cm^3, 3100 K, we varied the required bond lengths and times in order to determine that there is no sensitive dependence on a particular cutoff parameter. The results from this sensitivity study are shown in Fig. 1.6. The hydrogen–hydrogen is not shown as it made no difference. Each plot uses different carbon–carbon bond lengths, varied between 1.60 and 1.72 Å. The abscissa is the carbon–hydrogen bond length and is the same for all figures. Finally, the different colored lines denote different proximity time requirements from 60 to 120 fs. In a transient system such as this, as time goes to infinity, we expect the free carbon and free hydrogen to approach their atomic ratios (carbon to 33% and hydrogen to 66%). It can also be seen that there appear to be no clear breakpoints for picking one bond distance over another, hence using the pair correlation functions as a guide. If there were distinct features in Fig. 1.6, we would need to investigate the cause for them before continuing.

We use atom velocity as a guide to select a suitable duration. For this example, we used the kinetic theory of gasses and ideal gas law as a crude approximation to the velocity.

$$\frac{1}{2}mv^2 = \frac{3}{2}k_{\mathrm{B}}T$$

where k_{B} is the Boltzmann's constant, T is the absolute temperature, m is the mass (in our case of a single atom), and v is the average Maxwellian velocity. With $T =$ 3100 K, for carbon, we get a velocity of 2538 m/s or 0.02538 Å/fs. Therefore, over 100 fs, we can expect a single atom to move about 2.5 Å. For hydrogen, this would be about 25 Å. We assume that for C–H, the atoms must be bonded if the hydrogen does not rapidly move away from the carbon. Similarly, unless both carbons are moving parallel, they would still drift apart quickly enough to fail the time/distance

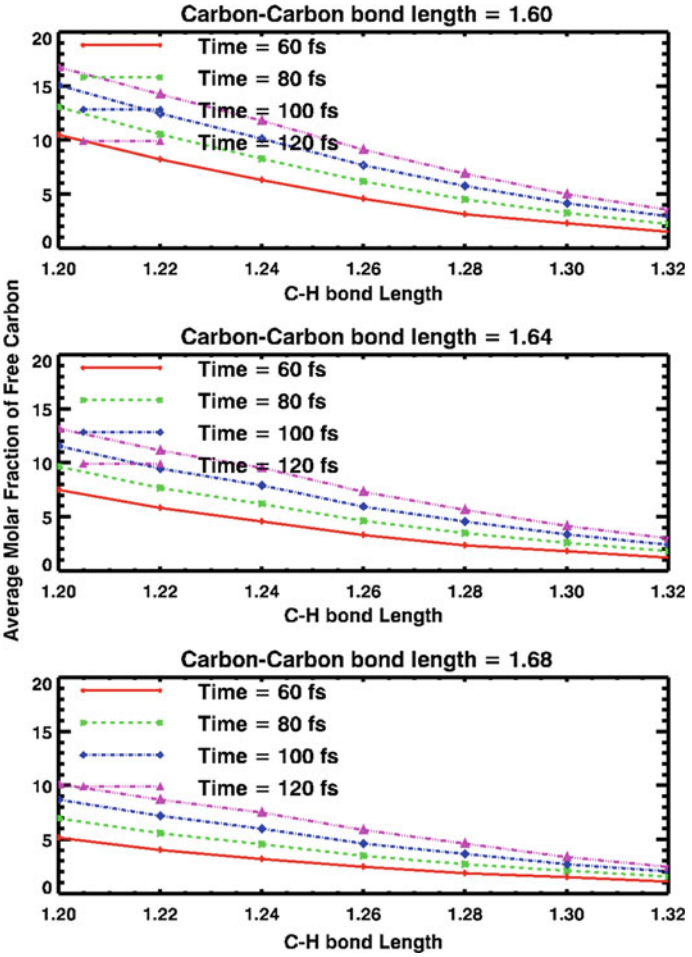

Fig. 1.6 Change in perceived composition as a function of bond distances for ethane at 1.5 g/cm^3 and 3100 K. The changes are smooth, so the selection of a particular bond cutoff does not change qualitative behavior

constraint. We use the vibrational period as a reference for our bond time calculation. A carbon–carbon triple bond has a full period of about 18 fs. For a double bond such as ethylene, the period is about 21 fs, and the period for a single bond in ethane is about 33 fs. The 100 fs time cutoff was chosen to be significantly longer than multiple vibration periods. The tracking method has a hard reset to a given molecule interaction meaning if two atoms move apart farther than the distance cutoff, they must satisfy the distance constraint for the entire time constraint again before they are considered bonded. This allows us to better distinguish between a scattering event and a bond.

After identifying all of the bonded atoms, we can begin to identify molecules. Our method uses a recursive algorithm capable of identifying branched molecules beyond a nearest-neighbor picture. One way to conceptualize this information is by building a three-dimensional construct where the first two dimensions are a matrix of atom-to-atom bonds (designated by either a 0 or 1 but more information can be stored) and the third dimension is time. The algorithm walks through the time-dependent upper diagonal, following all bonded pairs until no more bonds are found in that chain (at which point it starts with the next atom not in that chain) or until all atoms are accounted for.

The recursive nature of the algorithm makes it fast and reliable. The ability of looking beyond nearest neighbor is particularly important for the purpose of changing chemistry. In the case of polyethylene, the polymer structure is never recovered if cooled, but other species may be formed which helps us to understand how the system evolves from a metastable polymer to thermodynamic equilibrium along a given trajectory in a phase diagram.

Figure 1.7 shows the stoichiometry for four strands of polyethylene along the principle Hugoniot calculated according to the method described above. This series of simulations was performed with four strands of CH_2, 16 carbon atoms long and with an extra hydrogen atom at each end to cap the chain and prevent cross bonding (for a total of 200 atoms). For densities of 1.1 to 1.7 g/cm^3, all four strands are intact. At 2.6 g/cm^3, the system is almost entirely an atomic gas. Between 1.7 and 2.7 g/cm^3 is the dissociation regime responsible for the inflection in the Hugoniot. Outside of this regime, the stoichiometry is easy to calculate, but inside the variety and species of molecules is much harder to understand and additional constraints are often required, not on the bond tracking program itself but on the results. For example, one might

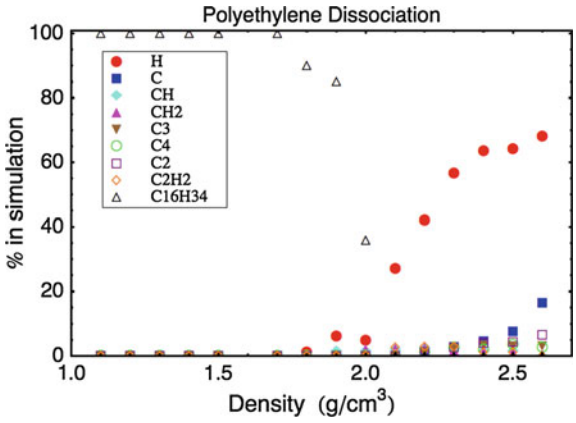

Fig. 1.7 Polyethylene stoichiometry along the principal Hugoniot. These simulations used 4 strands of 16 carbons and 32 hydrogens along the chain plus 2 hydrogens (one at each end) to cap the strand and prevent cross bonding. 1.1 g/cm^3 through 1.7 g/cm^3 show only $C_{16}H_{34}$ which indicates that all four strands are intact. At 2.6 g/cm^3 the system is almost entirely an atomic gas

see a C_1 and C_7H_5 for a few time steps and then see a C_2 and C_6H_5 for a few time steps. These are transients that do exist but are difficult to quantify in a meaningful way given the very small number of atoms present in a DFT simulation. Figure 1.7 shows only the most persistent of the species.

With this tool, we are able to carefully follow the dynamic chemistry of polymer dissociation as a function of shock strength. Accurate accounting of species is important for understanding the role of bond breaking in release of internal energy, for comparisons with classical molecular dynamics simulations using reactive force fields, and for comparison with chemical reactivity models.

1.3 Classical Molecular Dynamics Simulations of Polymers Under Shock Compression

DFT allows extremely high-fidelity descriptions of chemistry over a huge range of compressions; however, its system sizes are computationally constrained to just a few hundred atoms. This can be a significant obstacle, particularly in polymeric systems, where even single chains can easily exceed this number of atoms. Furthermore, in the case of structured polymers and foams, nanoscale features cannot be captured on length scales available to DFT. Thus, for the study of void collapse and hotspot heating, another simulation tool is required.

Classical molecular dynamics (MD) can extend the accessible simulation length scales to tens or hundreds of nanometers (and many millions to billions of atoms), by eliminating the electronic degrees of freedom and reducing quantum mechanical interactions into a classical ion–ion interatomic potential. These potentials are generally quantitatively accurate over smaller compression ranges than DFT, but can be highly accurate within these ranges.

Our classical MD simulations are run with Sandia's LAMMPS parallel molecular dynamics code [44]. LAMMPS allows highly efficient large-scale calculation and offers a broad library of established interaction potentials. For hydrocarbons, we have taken advantage of this library to compare the shock response of several published potentials under identical loading conditions.

In Mattsson et al. [38], we compared the results of two reactive and two bonded interatomic potentials. The reactive force fields, ReaxFF [7] and AIREBO [53] allow for chemical reactions and dissociation. The bonded force fields, OPLS-AA [21] and the Borodin et al. exponential-6 [4, 5] are computationally much more efficient but cannot capture dissociation reactions.

It had been expected that the reactive potentials would do better than the less sophisticated bonded potentials. However, we found that core stiffness was a stronger predictor of a potential's accuracy than its reactivity. Specifically, we found that the AIREBO and OPLS potentials were both too stiff in compression, and diverged from DFT and experiments well before the onset of dissociation chemistry. Since our 2010 study, however, both the AIREBO and OPLS potentials have been reworked to sig-

nificantly address the observed shortcomings in their high compression response. AIREBO-M [43] was refit to high-pressure graphene and polyethylene data, and now reproduces DFT results for shocked PE at least up to 40 GPa. Similarly, Sewell, Frohlich, and Thompson [13] showed how OPLS-AA can be refit to use exp-6 Buckingham-style interactions to replace the stiffer 12–6 Lennard-Jones cores. Given these improvements since our last comparison, we focus our discussion on the ReaxFF and Borodin potentials.

Shock compression states were produced using two MD methodologies. In the case of homogeneous full-dense polymer studies, the Hugoniostat [46] method was used to homogeneously bring the material to the final shock state. This equilibrium approach uses modified equations of motion to correlate the system compression to the internal energy thermostat, so as to enforce the RH relation, (1.3). For shocked foams, we used a full nonequilibrium (NEMD) propagating wave approach [20, 22] in order to capture the nonuniform dynamical collapse around the void spaces. NEMD uses a piston driver on one end of the system, to provide a sustained drive into the sample, producing a shock front, which then propagates across the system. Three representative ambient-density polymer systems are shown in Fig. 1.8. For these studies, we built polymeric systems from either polyethylene (PE) or poly(4-methyl 1-pentene) (PMP). While both materials have the same monomer C:H ratio of 1:2, and nearly identical local structure, they differ in extended structure. PE has a linear backbone, while PMP has a branched structure. Full-density systems for PE (0.930 g/cm^3, Fig. 1.8a), and PMP (0.801 g/cm^3, Fig. 1.8b) were built and equilibrated. In addition, the amorphous PMP was conducive to building distended foam systems (0.30 g/cm^3, Fig. 1.8c) as well. Details of the building and equilibration have been published [38, 49].

Figure 1.9 shows two plots of polymer Hugoniot response from Z experiments, DFT, and MD simulations. The MD simulations shown are for the ReaxFF and Borodin et al. potentials. We note that DFT best reproduces experiments over the full range of compression. The MD does reasonably well at lower compression but is generally stiffer than experimental measurements as pressure increases. In both the PE and PMP, the ReaxFF potential gives the better agreement with experiment between the two MD potentials shown. To within experimental uncertainty, it is accurate from ambient density up to approximately 2× ambient density. The Borodin potential is good from ambient up to ~1.6 g/cm^3. Moreover, the ReaxFF potential shows good agreement with DFT dissociation onset, as shown in Fig. 1.10, which begins at just above 1.8 g/cm^3 (vertical dashed line) in polyethylene. Figure 1.10 plots the percentage of carbon atoms bonded to two other carbons as a function of compression. This simple measure of polymer chemistry shows agreement between DFT and ReaxFF MD in both onset density and density trend to complete vaporization.

Based on Hugoniot response and dissociation, we conclude that MD with the ReaxFF potential gives comparable quantitatively accurate hydrocarbon simulations to DFT under compression up to ~1.8 g/cm^3. This validation allows us to extend atomistic simulations to length scales which are amenable to study of nanoscale foams.

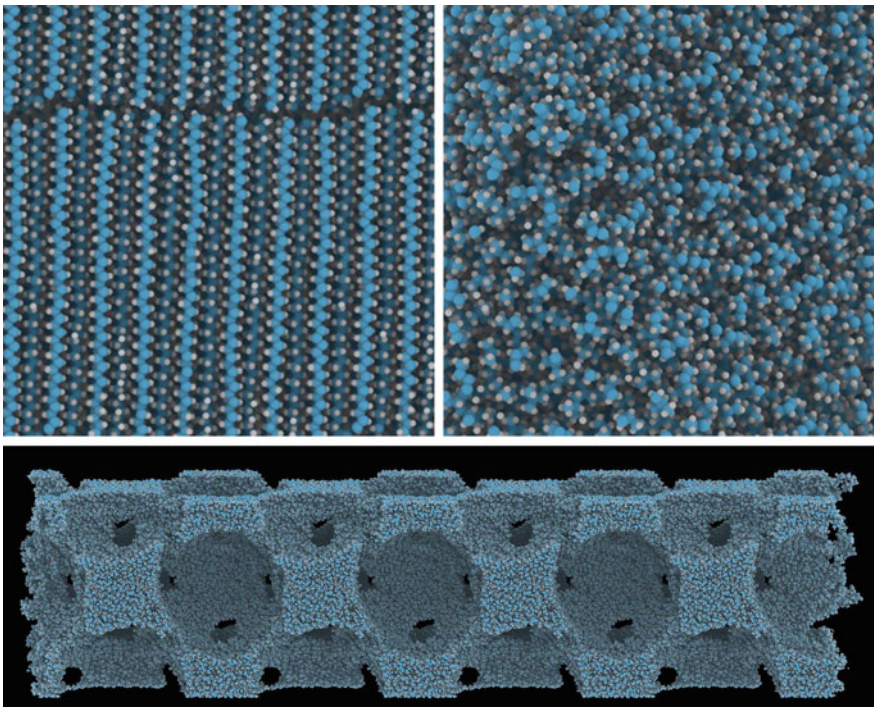

Fig. 1.8 Snapshots from initial configurations of molecular dynamics simulations for semicrystalline polyethylene (top left), poly(4-methyl 1-pentene), i.e., PMP (top right), and a model PMP foam with density of 0.30 g/cm^3 (bottom)

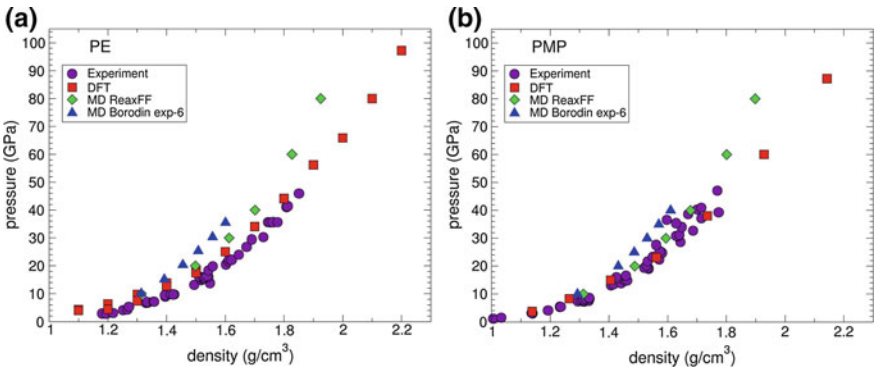

Fig. 1.9 Classical molecular dynamics Hugoniot response compared to experiments [36] and DFT data for full-density polyethylene (left) and Poly(4-methyl 1-pentene) (right) [38]

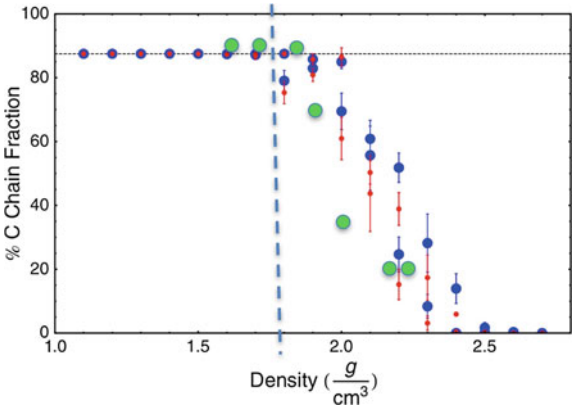

Fig. 1.10 Dissociation, as percent carbon chain, for DFT (20 and 50 fs bond criteria are blue and red, respectively) and ReaxFF classical MD (green) [38]. Maximum percent fraction is 87.5% for the C16 polyethylene chains, and 95% for the C44 chains, shown

While foams and porous materials are frequently useful and necessary in shaping high-pressure waves, their response is notoriously difficult to characterize. Experimental error bars are usually large due to sample-to-sample foam variation, as well as to inhomogeneities within individual samples. Issues of sample control combined with a lack of direct experimental measures of temperature and chemistry make analysis difficult. Root et al. conducted Z machine shock experiments on PMP foams with average density of 0.3 g/cm^3 [49]. The experimental results were published with extensive atomistic, and continuum simulations exploring the effects of porosity on average temperature, vaporization/ejecta, and wave propagation profiles. Subsequent work [30, 31] explored the temporal evolution of void collapse and local temperature hotspot formation.

A foam Hugoniot comparison between Z machine experiments, MD simulation, and Equation of State (EOS) calculations are shown in Fig. 1.11a. These results show that the final densities of these compressed systems do not reach nearly the compaction that the fully dense polymer samples reach these pressures. This is because the void collapse in foams leads to significant heating, which causes expansion in the final states. Because of this, we remain well within the density range for which ReaxFF has been shown to be reliable.

The Hugoniot curves for PMP foam have two distinct regions. At low pressures, the foam compacts to approximately four times its initial density, at which point the curve turns steeply vertical, with little increased density for large increases in pressure. In both the EOS calculations and the MD simulations, the data is tightly aligned along near-vertical lines. The experimental data, colored to match the same initial densities of MD and EOS data, have significant horizontal variation. The simulations help to build confidence for this being due to variation in foam density across different samples.

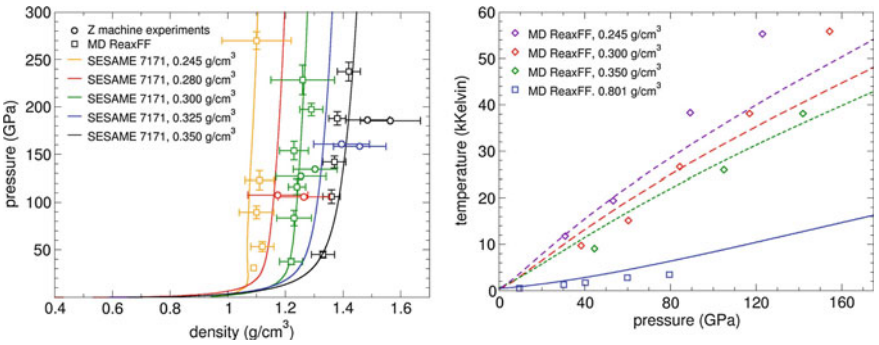

Fig. 1.11 Comparison of the shock Hugoniot from classical MD and experiments on Z [48, 49]. Equation of state results are also shown for SESAME 7171 [12, 19]

Figure 1.11b shows the final average temperatures for the same shot data. Experimental temperatures are not available. The data shows the strong dependence of final temperature on the initial density of the foam. The fully dense polymer temperatures are almost an order of magnitude lower than the foams. And the slope of increased temperature with pressure increases with decreasing initial density. This is consistent with the conclusion that increased void size/number leads to increasing hotspots and higher temperatures. One also sees in the plots that the MD temperatures show the same trends as the EOS temperatures and agree at lower pressures. However, at higher pressures, the SESAME 7171 values are consistently lower than MD temperatures, even when the pressure vs. density values agree. This is likely a result of the fact that the EOS model does not account for the polymer dissociation, which would indicate that the MD temperatures are more dependable. It should, however, be noted that these temperatures are well above the range usually explored with classical molecular dynamics.

The molecular dynamics snapshots in Fig. 1.12 demonstrate one significant mechanism, which was not observed in full-density polymer shock studies. We see significant vaporization and ejecta within the collapsing void. This vaporized material is produced at pressures and densities well below the onset of dissociation in dense polymer, because the temperatures in the collapsing voids are high enough to break bonds. Once the material is volatized, it can travel ballistically ahead of the shock front. In closed foams, these ejected particles impact the far side of the void, preheating the un-shocked material. In an open foam, the vaporized particles can travel far ahead of the shock front through the interconnected void space. The ejected particles travel at velocities as high as twice the bulk particle velocity. This observation explains features seen in the wave profiles. In both simulation and experiment, shock fronts are broader than expected, and the rise time of the front appears to be correlated to the void size.

These results indicate that classical molecular dynamics can be used effectively to model Z machine experiments in polymer shock compression. Specifically, with the right potentials, quantitative agreement can be made with DFT and experimental

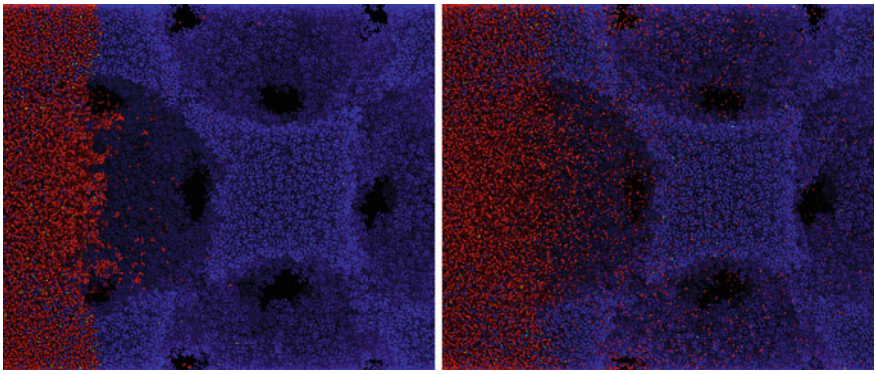

Fig. 1.12 Snapshots of a propagating shock front showing vaporized ejecta from the collapsing void. Atoms are colored by velocity in the shock direction. (left) piston velocity of 10 km/s, giving pressure of ~40 GPa (right), piston velocity of 25 km/s, giving pressure of ~240 GPa. Dissociated polymer is seen extending ahead of the shock front [31]

results over a useful range of compression. Moreover, because MD allows for the simulation of much larger features than those which can be captured with DFT, it can explore the mechanisms and processes associated with larger length scale structure in polymers (i.e., long-range order, defects, or voids). Moreover, aspects of the compression which are difficult or impossible to observe experimentally, including void collapse and temperature production, are readily studied with MD. For these reasons, classical molecular dynamics has proven to be a useful tool to augment our analysis and understanding of Z machine experiments.

1.4 Z Experiments on Polymer Materials

In the 1990s, Sandia researchers developed the Z machine as a pulsed power source for generating X-rays for radiation–material interaction studies and as an X-ray drive for experiments relevant for inertial confinement fusion studies [40, 52]. In 2007, the Z machine was refurbished [51] increasing the maximum current delivered to a target to approximately 20 MA in a pulse length of 100–600 ns making Z capable of producing magnetic pressures up to 600 GPa. Early on, researchers [15] determined that the current pulse could be used to drive a smoothly increasing compression wave into a target load where the time-dependent magnitude of the pressure loading is given as

$$P(t) = \frac{B^2(t)}{2\mu_0} = \mu_0 \frac{J^2(t)}{2} = \frac{\mu_0 I^2(t)}{2W(t)^2}$$

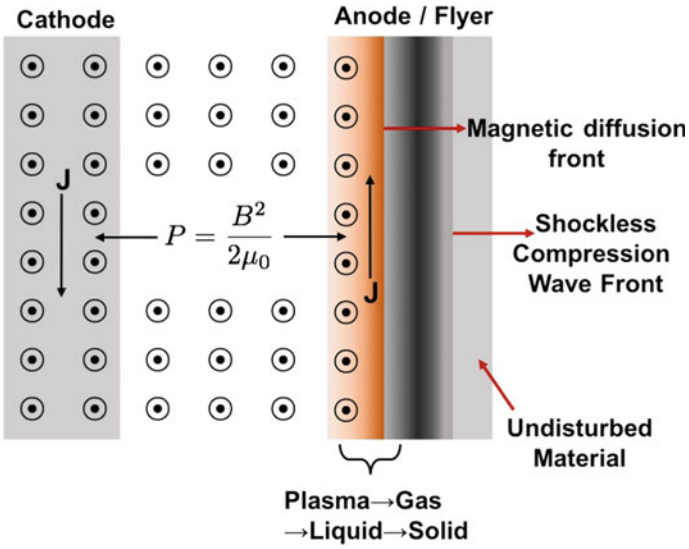

Fig. 1.13 Illustration of the current drive on the anode. The magnetic field penetrates only a fraction of the flyer, the shockless compression front outruns the magnetic field

where P is the pressure, $B(t)$ is the time-dependent magnetic field, $J(t)$ is the time-dependent current density in units of (amps/unit length), $I(t)$ is the time-dependent current, and $W(t)$ is a time-dependent scaling factor that depends on the load geometry. This led to the first shockless compression experiments to measure quasi-isentropes in materials [15]. From prior work at Sandia on the hyper-velocity launcher (HVL) gun using a shockless compression wave to launch flyer plates [8], the idea to use the Z machine to launch flyer plates was quickly conceived [16, 24].

Figure 1.13 shows the basic concept for either shockless compression or flyer plate experiments on Z. Current is driven in a loop along the anode and cathode through a shorting cap on the target's top. This current loop generates a magnetic field between the cathode and the anode. The combination of current and magnetic field creates a Lorentz force ($\vec{F} = \vec{J} \times \vec{B}$) that drives a shockless compression wave through the anode. A sample directly mounted to the anode will be shocklessly compressed as the compression wave transits into it. If the anode is left with a free surface, just as in the HVL, when the shockless compression wave reaches the anode free surface, the anode is accelerated outward from the cathode. Using a shockless compression wave minimizes the temperature rise in the anode, however, the high current causes Joule heating on the inner surface of the anode. This causes the conductivity to drop and the current begins to diffuse into the anode, which creates a magnetic diffusion front that propagates behind the compression wave front. The Joule heating melts and vaporizes the inner surface of the anode [10].

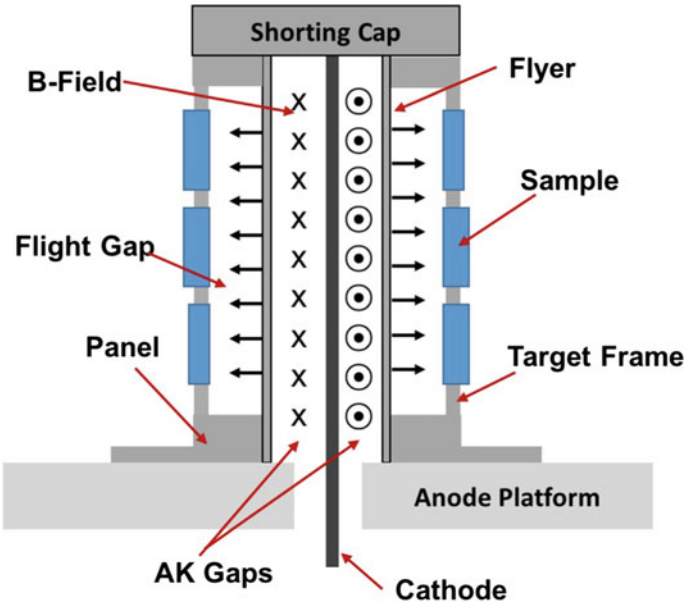

Fig. 1.14 Illustration of a Z coaxial geometry flyer plate experiment. The load is about 5 cm tall and 1 cm wide

The ability to shape the current pulse along with developments in 1D and 2D magnetohydrodynamics (MHD) simulations greatly improved the capabilities to use the Z machine for quasi-isentropic compression experiments [10] and for flyer plate experiments [32, 33]. By proper tailoring of the current pulse, the flyer plate is shocklessly accelerated to the desired velocity. Experiments are designed to ensure a steady shock through the sample and to avoid contamination in the measurement from release waves reflecting from Joule heated, melted portion of the flyer. Further refinements to the Z target geometry and improvements in MHD and Z circuit modeling have led to the successful launching of aluminum flyer plates up to around 40 km/s [34].

Figure 1.14 illustrates a rectangular target geometry used for flyer plate experiments. In this geometry, rectangular flyer plates are placed on opposite sides of the cathode. The flyer plates are typically aluminum, but Z has also used Al/Cu layered flyers where Cu is the impactor. The distance between the flyer plates and cathode, called the AK gap, is asymmetric—one side has a larger AK gap than the other side. This results in two different magnetic pressures that create two different flyer velocities on each side of the target, and thus, two different Hugoniot states in one experiment. MHD simulations are used to determine the flight gap so that the flyer plate reaches a terminal velocity prior to impact with the samples with a few hundred microns of solid density on the impact face [32, 33]. The target frame is designed to hold as many samples as possible to maximize the data return.

The Z machine has been used to study the high-pressure response of the hydrocarbon polymer: poly(4-methyl-1-pentene) plastics up to 985 GPa [50]. Poly(4-methyl-1-pentene) plastic (PMP) is a CH-based plastic in which the carbon atoms are sp^3-hybridized. PMP is often referred to by its trade name TPX® (Mitsui Chemicals, Inc.) and is available in several different variations. PMP is possible to machine and is transparent, which makes it a valuable window material for shock-release studies on the Z machine. For the work in [50], the PMP samples were the DX845 variant of TPX® with a density of 0.833 g/cm^3 and a melting temperature of 232 °C. The index of refraction of PMP is relatively constant over a large range of wavelengths. For the Z experiments, we use a 532 nm wavelength for our laser interferometry system. At that wavelength, PMP has an index of 1.461 ± 0.001.

The laser interferometry system at Z is a velocity interferometer system for any reflector (VISAR) that was originally developed at Sandia National Laboratories in the late 1960s and early 1970s. Details of the VISAR technique for shock wave research are found in [2, 3, 14, 17]. The VISAR measures flyer plate velocities and shock velocities during the Z experiment.

Figure 1.15 shows a schematic illustration of the experimental configuration along with two sample VISAR measurements. An aluminum flyer plate is accelerated toward the PMP samples. Two different sample configurations were used for measuring the high-pressure response of PMP (*inset)*: the top configuration is a thick sample of PMP used to measure the Hugoniot. The bottom configuration is a PMP/quartz window stack used to measure the Hugoniot and the reshock state in PMP. In the experiment, VISAR tracks the flyer plate trajectory, directly measuring the flyer plate velocity up to impact. The flyer plates are shocklessly accelerated to the desired velocity. At impact, a shock is produced in the PMP sample. The shock strength is high enough that the shock front in the PMP becomes reflective and the VISAR laser reflects off the shock front. This allows for a direct, precise measurement of the shock velocity as the shock wave travels through the sample.

Figure 1.15 (red) shows the shock through the PMP is steady for 10 s of ns. At late times in the single PMP sample, the velocity begins to decrease. The velocity decrease is caused by reflected release waves from the melted portion of the flyer (Fig. 1.13). In the quartz backed PMP configuration, a steady wave is observed in the quartz for 10 s of ns as well. At later times, a second shock is observed in the quartz. This is caused by the reflected shock from the PMP/quartz interface and the PMP/aluminum impactor interface. Again, release waves from the melted portion of the flyer cause the decrease in the shock velocity.

The advantage to using the Z machine is that it launches solid density flyers at the targets. Thus, the flyer plate is well characterized at impact. Combined with the direct measurement of the shock velocity in the PMP, the Hugoniot state is easily and accurately determined through impedance matching [6]. A *Monte Carlo* impedance matching (MCIM) method [50] is used to calculate the Hugoniot state and uncertainty. The MCIM method accounts for uncertainty in the measurements, initial densities, and the uncertainty in the Hugoniot of the flyer plate. Figure 1.16 shows the compiled Hugoniot data for PMP along with the QMD calculated Hugoniot for PMP discussed earlier in the chapter.

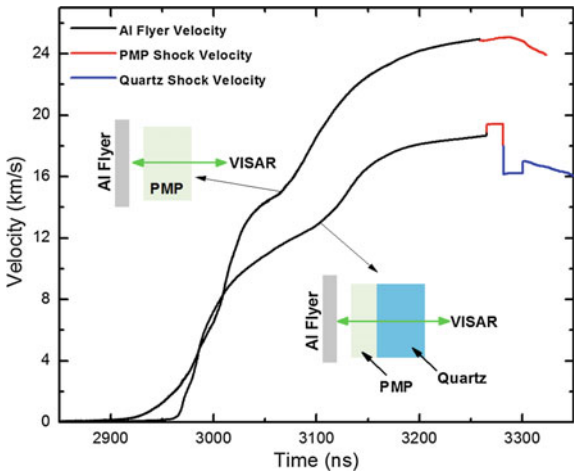

Fig. 1.15 VISAR measured velocity traces from two different experiments on PMP plastics showing the flyer velocity, PMP shock velocity, and the quartz shock velocity. Inset: Configuration for experiments using the direct shock experiment (top sample) and the shock—reshock experiment (bottom sample)

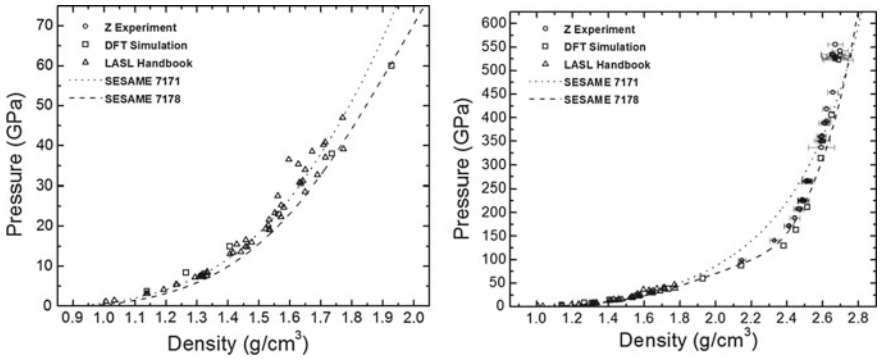

Fig. 1.16 Hugoniot of PMP plastic in density–pressure space. The left panel shows the low-pressure range where there was previous data. The QMD simulations are in excellent agreement with data over a large range

Figure 1.16 shows the Z experimental data range from 100 to 550 GPa along the principal Hugoniot. The QMD calculations are in good agreement up to 400 GPa. Starting at about 150 GPa, the principal Hugoniot steepens dramatically compared to the Hugoniot below 100 GPa. The sharp upturn suggests dissociation of the molecular system into an atomic system. This similar behavior along the Hugoniot was observed in the molecular systems of CO_2 [48, 49] and ethane (C_2H_6) [35].

The bond tracking analysis method discussed earlier was used to assess dissociation along the Hugoniot. Figure 1.17 shows the results of the bond tracking analysis. At low shock pressures of approximately 20 GPa, the polymer chain begins to break

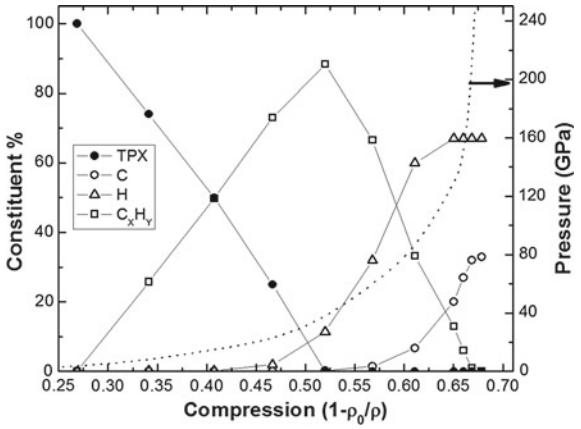

Fig. 1.17 Analysis of the atomic species of shocked PMP using the bond tracking analysis method

down and complex C_xH_y constituents are observed. Increasing the shock pressure increased the amount of free hydrogen. At a shock pressure of approximately 150 GPa, all H atoms have dissociated from the C chains and the number of free C atoms begins to increase. Complete dissociation into C and H atoms requires a shock pressure of approximately 315 GPa.

At 315 GPa, the compression factor $\mu = 1 - \rho_0/\rho$ is $\mu = 0.68$. At 160 GPa where the system is primarily atomic C and H with a small percentage (~6%) of C–C clusters, $\mu = 0.66$. Interestingly, this compression factor of $\mu = 0.66$–0.68 for complete dissociation is consistent with other C–H systems with sp^3-hybridized bonded carbon. Complete dissociation for ethane (C_2H_6) occurs at $\mu = 0.69$ [35], for polyethylene $\mu = 0.62$ [9], and polystyrene $\mu = 0.62$ [54]. For each system, the pressure and temperature at complete dissociation are different, but the compression factors are all similar. This suggests that the C–C bonds are more affected by compression than pressure or temperature since compression reduces the gap between bonding and anti-bonding orbitals making it easier to occupy the anti-bonding states in the C.

1.5 Summary and Conclusions

Hydrocarbon polymers are commonly used in shock physics research, and their behavior is complex. Strong compression of hydrocarbon polymers involves a series of physical mechanisms, together resulting in the Hugoniot response shown in Fig. 1.2. Under progressively stronger shock loading, the hydrocarbon polymers discussed in this chapter (linear polyethylene and polymethylpentene with side chains) first respond softly as the void space between polymer chains is compressed resisted only by the relatively weak inter-molecular Van der Waals interaction. During this phase, the covalent bonds of the polymer remain intact (Fig. 1.7). Once the voids

space has been removed, the atomic repulsion becomes progressively stronger, the temperature continues to increase, and the polymer melts. Upon further compression, dissociation of the polymer occurs over a range in density, pressure, and temperature (Fig. 1.7). The breaking of covalent bonds cost significant energy, resulting in a distinct plateau in the Hugoniot (Figs. 1.2 and 1.16). As the pressure, temperature, and density increase even further, dissociation is complete with the system now being comprised of free atoms. Beyond dissociation, the pressure and temperature of the final shock state rise very steeply with increased shock strength and the state turns into a dense strongly coupled plasma of hydrogen and carbon.

In this chapter, we have shown how to utilize different simulation techniques to interrogate and understand the behavior of two polymers under shock compression. The results from simulations are compared to experimental data from Sandia's Z machine and found to be in qualitative and quantitative agreement. First, molecular dynamics based on density functional theory is used to calculate thermodynamic final states that are in quantitative agreement with high-precision experiments executed on Sandia's Z machine; second, the DFT/QMD simulations are employed to analyze how the molecular structure changes with increasing shock pressure; third DFT/QMD simulations are used to determine the range of validity of model potentials commonly used in classical MD simulations; and fourth classical MD simulations are applied to nonequilibrium conditions to explore the effect of structure like voids.

We conclude that it is possible to model shock compression of polymers with high fidelity for a range of shock strengths when using DFT/QMD and that classical MD simulations provide valuable insights into the shock compression dynamics of mesoscale materials like polymer foams.

Acknowledgements We sincerely thank our many collaborators and colleagues who have inspired or contributed to the EOS work presented in this chapter, including Gary Grest, Mike Desjarlais, Ronald Redmer, Marcus Knudson, Tracy Vogler, Tom Haill, Ray Lemke, Aidan Thompson, Flint Pierce, Diana Schroen, Rudy Magyar, Ann Mattsson-Wills, John Carpenter, Luke Shulenburger, Dan Dolan, Martin French, Mark Herrmann, John Benage, and Dawn Flicker.
We also thank the large team of staff and management operating the Z machine and target fabrication. The work was supported by the NNSA Science Campaigns. This paper describes objective technical results and analysis. Any subjective views or opinions that might be expressed in the paper do not necessarily represent the views of the U.S. Department of Energy or the United States Government. Sandia National Laboratories is a multimission laboratory managed and operated by National Technology and Engineering Solutions of Sandia, LLC., a wholly owned subsidiary of Honeywell International, Inc., for the U.S. Department of Energy's National Nuclear Security Administration under contract DE-NA-0003525.

References

1. Allen, Tildesley (1990) Computer simulations of liquid. Cambridge University Press
2. Barker LM, Hollenbach RE (1972) J Appl Phys 43:4669
3. Barker LM, Schuler KW (1974) J Appl Phys 45:3692
4. Borodin O, Smith GD (2006) J Phys Chem B 110:6279
5. Borodin O, Smith GD, Bedrov D (2002) J Phys Chem B 106:9912

6. Boslough MB, Asay JR (1993) In: Asay JR, Shahinpoor M (eds) High-pressure shock compression of solids. Springer, New York, p 7
7. Chenoweth K, van Duin ACT, Goddard WA III (2008) J Phys Chem A 112:1040
8. Chhabildas LC, Kmetyk LN, Reinhart WD, Hall CA (1995) Int J Impact Eng 17:183
9. Cochrane Kyle R, Desjarlais Michael, Mattsson Thomas R (2012) AIP Conf Proc 1426:1271
10. Davis J-P, Deeney C, Knudson MD, Lemke RW, Pointon TD, Bliss DE (2005) Phys Plasmas 12:056310
11. Desjarlais MP (2003) Phys Rev B 68:064204
12. Dowell F (1982) Technical report no LA-9559-MS, Los Alamos National Laboratory, Los Alamos, NM
13. Fröhlich MG, Sewell TD, Thompson DL (2014) J Chem Phys 140:024902
14. Goosman DR (1975) J Appl Phys 46:3516
15. Hall CA (2000) Phys Plasmas 7:2069
16. Hall CA, Knudson MD, Asay JR, Lemke RW, Oliver B (2001) Int J Impact Eng 26:275
17. Hemsing WF (1979) Rev Sci Instrum 50:73
18. Hohenberg P, Kohn W (1964) Phys Rev 136:B864
19. Holian KS (1984) Technical report no LA-10160-MS, Los Alamos National Laboratory, Los Alamos, NM
20. Holian BL, Lomdahl PS (1998) Science 280:2085
21. Jorgensen WL, Maxwell DS, Tirado-Rives J (1996) J Am Chem Soc 118:11225
22. Kadau K, Germann TC, Lomdahl PS, Holian BL (2002) Science 296:1681
23. Knudson MD et al (2001) Phys Rev Lett 87:225501
24. Knudson MD, Hall CA, Lemke RW, Deeney C, Asay JR (2003) Int J Impact Eng 29:377
25. Knudson MD, Desjarlais MP, Dolan DH (2008) Science 322:1822
26. Knudson MD, Desjarlais MP (2009) Phys Rev Lett 118:035501
27. Knudson MD, Desjarlais MP (2009) Phys Rev Lett 103:225501
28. Knudson MD et al (2012) Phys Rev Lett 108:091102
29. Kohn W, Sham LJ (1964) Phys Rev 140:A1133
30. Lane JMD, Grest GS, Thompson AP, Cochrane KR, Desjarlais MP, Mattsson TR (2012) AIP Conf Proc **1426**, 1435
31. Lane JMD, Grest GS, Mattsson TR (2013) Comput Mater Sci 79:873
32. Lemke RW, Knudson MD, Hall CA, Haill TA, Desjarlais MP, Asay JR, Mehlhorn TA (2003) Phys Plasmas 10:1092
33. Lemke RW, Knudson MD, Bliss DE, Cochrane K, Davis J-P, Giunta AA, Harjes HC, Slutz SA (2005) J Appl Phys 98:073530
34. Lemke RW, Knudson MD, Davis J-P (2011) Int J Impact Eng 38:480
35. Magyar RJ, Root S, Cochrane K, Mattsson TR, Flicker DG (2015) Phys Rev B 91:134109
36. Marsh SP (ed) (1980) LASL shock Hugoniot data University of California Press, Berkeley
37. Mattsson AE, Schultz PA, Desjarlais MP, Mattsson TR, Leung K (2005) Model Simul Mater Sci Eng 13:R1
38. Mattsson TR, Lane JMD, Cochrane KR, Desjarlais MP, Thompson AP, Pierce F, Grest GS (2010) Phys Rev B 81:054103
39. Mattsson TR et al (2014) Phys Rev B 90:184105
40. Matzen MK (1997) Phys Plasmas 4:1519
41. Matzen MK et al (2005) Phys Plasmas 12:055503
42. Mermin N (1965) Phys Rev 137:A1441
43. O'Connor TC, Andzelm J, Robbins MO (2015) J Chem Phys 142:024903
44. Plimpton S (1995) J Comp Phys **117**(1). http://lammps.sandia.gov
45. Prisbrey ST et al (2012) Phys Plasmas 19:056311
46. Ravelo R, Holian BL, Germann TC, Lomdahl PS (2004) Phys Rev B 70:014103
47. Root S et al (2010) Phys Rev Lett 105:085501
48. Root S, Cochrane KR, Carpenter JH, Mattsson TR (2013) Phys Rev B 87:224102
49. Root S, Haill TA, Lane JMD, Thompson AP, Grest GS, Schroen DG, Mattsson TR (2013) J Appl Phys 114:103502

50. Root S, Mattsson TR, Cochrane K, Lemke RW, Knudson MD (2015) J Applied Physics 118:205901
51. Savage ME et al (2007) In: Proceedings of the IEEE pulsed power conference, vol 1–4, p 979
52. Spielman RB et al (1996) In: Proceedings of the 11th international conference on high-power particle beams, vol 150
53. Stuart SJ, Tutein AB, Harrison JA (2000) J Chem Phys 112:6472
54. Wang C, He XT, Zhang P (2011) Phys Plasmas 18:082707